MDPI

Article

Wet Chemical Synthesis of $Al_xGa_{1-x}As$ Nanostructures: Investigation of Properties and Growth Mechanisms

Yana Suchikova [1], Sergii Kovachov [1], Ihor Bohdanov [1], Marina Konuhova [2], Yaroslav Zhydachevskyy [1,3], Kuat Kumarbekov [4], Vladimir Pankratov [2] and Anatoli I. Popov [2,4,*]

[1] The Department of Physics and Methods of Teaching Physics, Berdyansk State Pedagogical University, 71100 Berdyansk, Ukraine; ya_suchikova@bdpu.org.ua (Y.S.); essfero@gmail.com (S.K.); rector_bdpu@ukr.net (I.B.); zhydach@ifpan.edu.pl (Y.Z.)

[2] Institute of Solid State Physics, University of Latvia, 8 Kengaraga, 1063 Riga, Latvia; marina.konuhova@cfi.lu.lv (M.K.); vpank@latnet.lv (V.P.)

[3] Institute of Physics, Polish Academy of Sciences, al. Lotnikow 32/46, 02-668 Warsaw, Poland

[4] Faculty of Physics and Technical Sciences, L.N. Gumilyov Eurasian National University, Astana 010008, Kazakhstan; kumarbekov@inbox.ru

* Correspondence: popov@latnet.lv

Abstract: This study focuses on the wet chemical synthesis of $Al_xGa_{1-x}As$ nanostructures, highlighting how different deposition conditions affect the film morphology and material properties. Electrochemical etching was used to texture GaAs substrates, enhancing mechanical adhesion and chemical bonding. Various deposition regimes, including voltage switching, gradual voltage increase, and pulsed voltage, were applied to explore their impact on the film growth mechanisms. SEM analysis revealed distinct morphologies, EDX confirmed variations in aluminum content, Raman spectroscopy detected structural disorders, and XRD analysis demonstrated peak position shifts. The findings emphasize the versatility and cost-effectiveness of wet electrochemical methods for fabricating high-quality $Al_xGa_{1-x}As$ films with tailored properties, showing potential for optoelectronic devices, high-efficiency solar cells, and other advanced semiconductor applications.

Keywords: $Al_xGa_{1-x}As$; wet chemical synthesis; electrochemical deposition; morphology; electrochemical etching; SEM; EDX; Raman spectroscopy; XRD; semiconductors

Citation: Suchikova, Y.; Kovachov, S.; Bohdanov, I.; Konuhova, M.; Zhydachevskyy, Y.; Kumarbekov, K.; Pankratov, V.; Popov, A.I. Wet Chemical Synthesis of $Al_xGa_{1-x}As$ Nanostructures: Investigation of Properties and Growth Mechanisms. *Crystals* **2024**, *14*, 633. https://doi.org/10.3390/cryst14070633

Academic Editor: Benilde F. O. Costa

Received: 31 May 2024
Revised: 5 July 2024
Accepted: 7 July 2024
Published: 9 July 2024

Copyright: © 2024 by the authors. Licensee MDPI, Basel, Switzerland. This article is an open access article distributed under the terms and conditions of the Creative Commons Attribution (CC BY) license (https://creativecommons.org/licenses/by/4.0/).

1. Introduction

The rapid development of electronics and photonics continually drives the search for new materials that offer precise control over their properties [1–3]. In this pursuit, tandem heterostructures [4,5] have garnered significant attention due to their ability to enhance device performance across various applications [6–8]. Among these materials, heterostructures based on cadmium-telluride (CdTe) [9,10] semiconductors, cadmium oxide (CdO) [11,12], and indium-gallium-selenide (InGaSe) [13,14] have been extensively studied and documented in the literature for their unique electronic and optical properties.

Cadmium-telluride semiconductors, for example, are widely used in photovoltaic cells due to their suitable bandgap for solar energy absorption and high conversion efficiency [15,16]. Cadmium oxide is utilized in transparent conductive films for touch screens, solar cells, and flat panel displays [17,18]. CuGaInSe has been chosen for thin-film solar cell production due to its high absorption coefficient and tunable bandgap, allowing better solar light capture than traditional silicon cells [19,20].

Despite their broad application and significant advantages, these materials' mass production and broader implementation face several critical challenges. The raw material costs for these semiconductors often remain prohibitively high, limiting their use to niche applications where performance outweighs cost considerations [21,22]. Moreover, the potential and apparent toxicity of materials such as cadmium poses substantial environmental

and health risks, leading to stringent regulations and a push for safer alternatives [23,24]. This is particularly relevant for cadmium-telluride, where the toxicity of cadmium compounds creates disposal and health issues during manufacturing and at the end of product life [25,26].

Additionally, the complexity of synthesis technologies for these materials adds another layer of challenge. Synthesis processes often require high precision, complex equipment, and controlled environments to achieve the desired material quality and properties [27,28]. These factors contribute to higher production costs and technical barriers that further impede their widespread adoption [29].

In contrast to these materials, developing ternary compounds based on gallium-aluminum offers a more sustainable and less problematic solution [30,31]. These materials offer similar advancements in electronic and photonic applications but with potentially lower toxicity and more straightforward synthesis procedures [32,33]. The ability to control the properties of $Al_xGa_{1-x}As$ by adjusting the aluminum content allows for precise tuning of its electronic and optical characteristics, making it an attractive alternative for applications ranging from high-efficiency photovoltaic cells to lasers and light-emitting diodes [34–36]. This versatility, combined with the more benign nature of the constituent materials, presents compelling arguments for its expanded use in the semiconductor industry [37].

In the context of semiconductor materials and their applications, $Al_xGa_{1-x}As$ structures demonstrate clear advantages, making them particularly attractive for a range of electronic and photonic applications. For example, $Al_xGa_{1-x}As$ alloys provide excellent thermal stability [38] and good chemical resistance [39], which are critical for high-power and high-frequency devices [40,41]. This stability ensures that materials maintain their performance characteristics under various environmental conditions and over extended operational periods, thereby enhancing the reliability and lifespan of devices [42,43].

The versatility of $Al_xGa_{1-x}As$ in device fabrication is another significant advantage [44,45]. It can be utilized in various device structures, including heterojunction bipolar transistors (HBTs) [46], high-electron-mobility transistors (HEMTs) [47], and complex multilayer structures for solar cells [48]. This versatility, combined with the ability to grow high-quality films using methods such as molecular beam epitaxy (MBE) [49] and metal-organic chemical vapor deposition (MOCVD) [50], enables the exploration of new device architectures. However, the complexity and cost associated with these methods present significant barriers, particularly in terms of investment in equipment, operational costs, and the need for highly specialized technical expertise [51,52].

Electrochemical wet methods present a promising alternative to synthesizing these heterostructures [53–56]. These methods are less expensive and less complex, making them more accessible for a broader range of applications and research environments [57,58]. Unlike MBE and MOCVD, which require high vacuum conditions and complex control systems, electrochemical methods can be conducted at room temperature and atmospheric pressure, significantly reducing infrastructure and energy requirements [59–62].

One of the compelling advantages of electrochemical deposition is its versatility in forming not only uniform films but also complex surface nanostructures [63–66]. This capability arises from the ability to dynamically adjust deposition parameters such as electrolyte composition, current density, and voltage, which influence the nucleation and growth kinetics of the deposited material [67,68]. By manipulating these parameters, nanostructured surfaces that enhance the functional properties of heterostructures [69,70] are possible.

Nanostructured surfaces offer competitive advantages, especially optoelectronic and photovoltaic applications [71,72]. For instance, nanostructures like quantum dots and nanowires can be directly integrated into devices to improve light absorption and emission properties [73,74]. In solar cells, the increased surface area provided by nanostructures enhances light harvesting efficiency, leading to higher energy conversion efficiencies [75,76]. Similarly, nanostructures can modify the light emission profile in LEDs and laser diodes and improve device extraction efficiency [77].

Furthermore, the ability to form nanostructured surfaces using electrochemical methods can also lead to the development of new device architectures that are not feasible with traditional flat-layer deposition methods [78]. For example, the development of graded composition and bandgap profiles achieved through controlled electrochemical deposition can be used to create multijunction solar cells with optimized bandgap profiles for efficient solar energy conversion across the solar spectrum [79,80].

In this paper, we investigate the impact of electrochemical deposition conditions, including applied potential, duration, and the number of treatment cycles, on the characteristics of deposited nanolayers. Specifically, we explore how these variables affect the morphological, compositional, phase, and photoluminescent properties of $Al_xGa_{1-x}As$ heterostructures synthesized on textured GaAs substrates. This study aims to elucidate the relationship between deposition parameters and the resulting material properties through detailed analysis, thereby providing insights into optimizing electrochemical processes for semiconductor device fabrication.

2. Materials and Methods

$Al_xGa_{1-x}As$ was formed on the surface of textured GaAs using wet electrochemical deposition, and the surface texturing of GaAs was carried out by wet electrochemical etching.

2.1. Experimental Setup

A standard three-electrode electrochemical cell was used for the electrochemical etching and deposition processes required to synthesize $Al_xGa_{1-x}As$ heterostructures (Figure 1). The electrodes were arranged parallel to each other and perpendicular to the bottom of the cell, maintaining a uniform distance of 1 cm between them. This arrangement ensures a uniform electric field distribution in the electrolyte, promoting a consistent deposition or etching process. A standard silver/silver chloride (Ag/AgCl) electrode was used as the reference electrode, providing a stable reference potential for controlling and monitoring the electrochemical reactions.

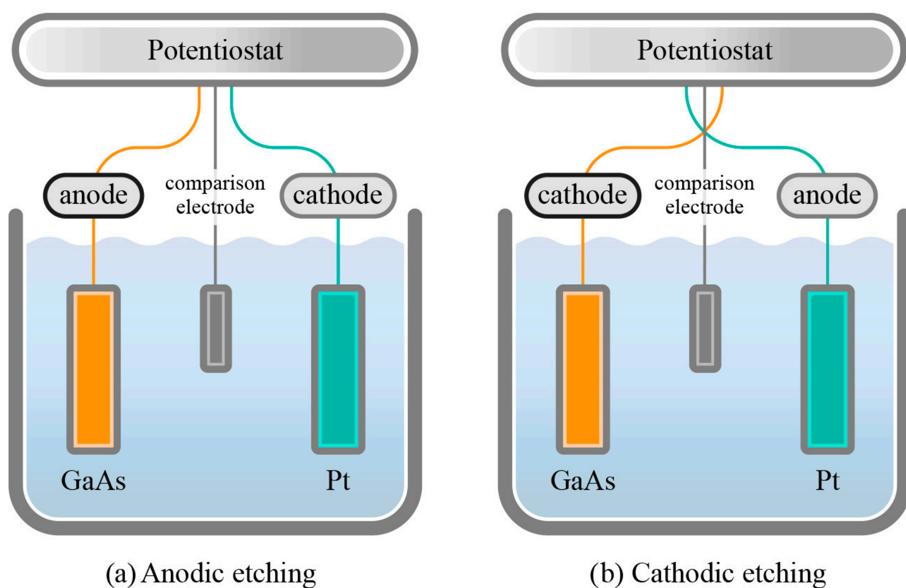

Figure 1. Experimental setup: (**a**) Anodic electrochemical etching mode; (**b**) Cathodic electrochemical deposition mode.

2.1.1. Electrochemical Etching Configuration

During the electrochemical etching phase, the setup used a gallium arsenide (GaAs) sample as the anode. The cathode consisted of platinum, a stable and inert counter-electrode (Figure 1a). This configuration ensures that the etching process is focused on the GaAs substrate, modifying its surface without contaminating the cathode. In this config-

uration, etching is an anodic reaction, where the GaAs substrate is oxidized, selectively removing material.

2.1.2. Electrochemical Deposition Configuration

The cell configuration was adjusted for the electrochemical deposition process. In this mode, the platinum electrode served as the anode, and the textured GaAs sample acted as the cathode (Figure 1b). This role change facilitates the deposition of the $Al_xGa_{1-x}As$ layer on the GaAs substrate by attracting positively charged particles from the electrolyte to the negatively charged substrate, thereby characterizing this process as a cathodic reaction.

2.1.3. Environmental Conditions

Given the materials' photosensitivity, all experiments were conducted in the dark to avoid any photochemical reactions or interference caused by light. The temperature was maintained at room temperature, providing a stable thermal environment to prevent changes in reaction kinetics or material properties induced by temperature fluctuations.

2.2. Samples for the Experiment

This study's experimental substrates consisted of monocrystalline gallium arsenide (GaAs) n-type wafers grown using the Czochralski method [81,82]. These substrates were cut into 10 mm by 20 mm pieces with a thickness of approximately 0.5 mm. The sample surfaces were oriented along the (111) plane. The samples were cut into ingots measuring 1 mm × 2 mm × 0.2 mm. These mono-GaAs samples have the following characteristics: conductivity type is n-type, doped with Sb, and have a carrier concentration of 2.3×10^{18} cm^{-3}. The orientation of the crystal is (111) with a face-centered cubic crystal lattice, commonly known as the zinc blende structure. The atomic density is 4.43×10^{22} cm^{-3}. The space group is $F\overline{4}3m$, and the band gap is 0.19 eV. The predicted formation energy is -0.446 eV/atom, and the density is 5.05 g·cm^{-3}. Figure 2 shows SEM, EDX, Raman, and XRD analyses of the single-crystal GaAs. These measurements confirm the single-crystalline quality and provide a comprehensive baseline characterization of the substrate.

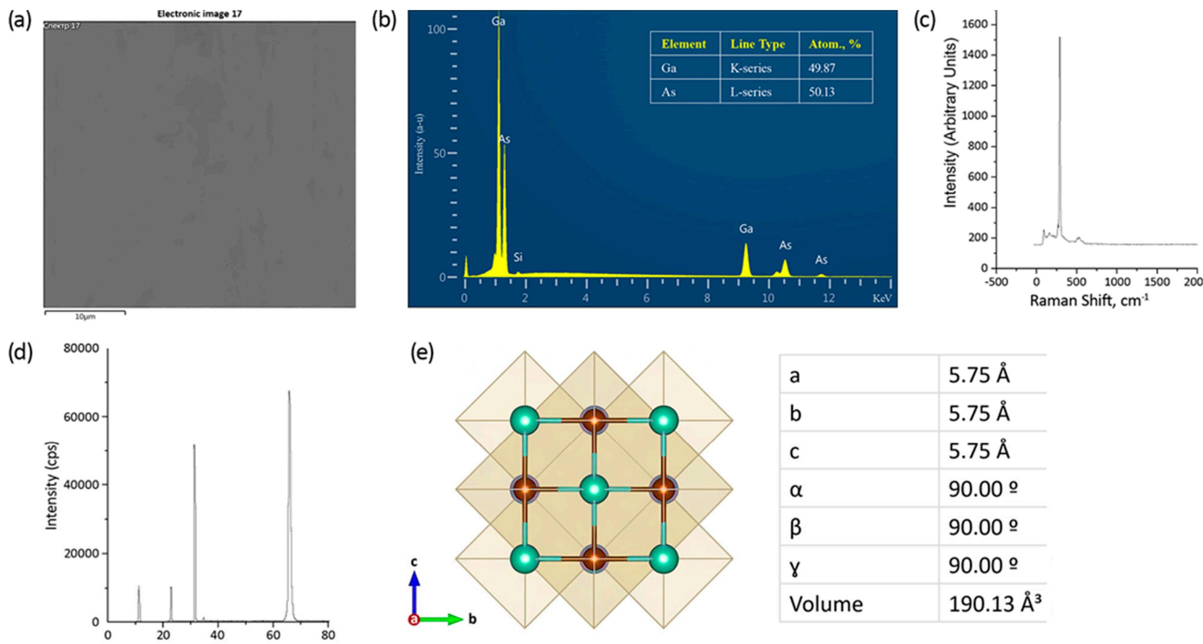

Figure 2. Characterization of single-crystal GaAs substrates used in the study: (**a**) SEM image of the unetched GaAs substrate showing a smooth, uniform surface indicative of single crystallinity;

(**b**) EDX spectrum confirming the elemental composition of the GaAs substrate; (**c**) Raman spectrum showing the characteristic peaks of single-crystal GaAs; (**d**) XRD pattern of the GaAs substrate confirming its single-crystalline nature with sharp, well-defined peaks; (**e**) schematic image and crystal lattice parameters GaAs.

Before deposition, the samples underwent a series of cleaning and preparation steps. Initially, they were mechanically polished using aluminum oxide powder to achieve a smooth, defect-free surface. After polishing, they were thoroughly cleaned to remove residual particles and contaminants. This cleaning involved rinsing the samples in a solution of hydrochloric acid and hydrogen peroxide ($HCl{:}H_2O_2$) in a 3:1 volume ratio.

2.3. Formation of Textured GaAs Layer

To enhance the adhesion of the deposited $Al_xGa_{1-x}As$ layer, the gallium arsenide (GaAs) samples were subjected to an electrochemical etching process before deposition. This etching created a textured layer on the GaAs substrates, promoting better mechanical interlocking and chemical bonding with subsequent $Al_xGa_{1-x}As$ layers.

The electrochemical etching was carried out by immersing the GaAs samples in a solution of nitric acid (HNO_3) and water (H_2O) in a 1:3 volume ratio. The etching process was conducted under a controlled voltage of 5 volts for 3 min. This condition was optimized to achieve uniform surface texturing without excessive etching or the formation of porous layers.

The primary goal was to create a microscopically rough surface on the GaAs substrates. This texturing significantly increases the surface area available for bonding, which is crucial for the subsequent deposition of the $Al_xGa_{1-x}As$ layer. The textured surface provides numerous nucleation sites that facilitate uniform film growth and enhance the structural integrity of the heterostructure.

Figure 3 shows the textured surface of the gallium arsenide (GaAs) layer subjected to electrochemical etching in preparation for the subsequent deposition of $Al_xGa_{1-x}As$ films. While the etched surface may exhibit features that resemble polycrystallinity, this results from the electrochemical etching process, which creates a textured surface to enhance adhesion. The underlying substrate remains monocrystalline. The texturing process formed rectangular, misoriented crystallites of varying sizes, heights, and degrees of inclination across the surface. The crystallites exhibit a somewhat irregular arrangement, creating a rough and uneven topography, ideal for enhancing mechanical interlocking and chemical adhesion with the deposited layers.

The surface also exhibits traces of cracking, which is particularly important in semiconductor fabrication. These cracks indicate the release of dislocations in the crystalline structure. While cracking is generally considered detrimental, in this scenario, it may be beneficial by reducing internal stresses within the substrate. Such stress relief is crucial when additional layers are deposited onto the substrate. Minimizing stress between the GaAs substrate and the $Al_xGa_{1-x}As$ layers, these cracks help prevent the formation of new dislocations and other defects during subsequent layer growth. The cracks indicate the release of dislocations in the crystalline structure, a phenomenon commonly associated with electrochemical etching. These surface features result from the texturing process designed to enhance film adhesion and do not reflect the bulk crystalline nature of the GaAs substrate, which remains monocrystalline.

The etching process enhances the mechanical adhesion between the deposited Al_xGa_{1-x} As layer and the GaAs substrate by increasing the surface roughness. Microscopic-scale bonding of the layers creates a more stable and durable heterostructure. Texturing helps reduce the formation of interfacial defects, such as dislocations and voids, that can arise from lattice mismatch or differences in thermal expansion between the GaAs substrate and the $Al_xGa_{1-x}As$ film. Minimizing these defects is crucial for improving the electronic and optical properties of the heterostructure.

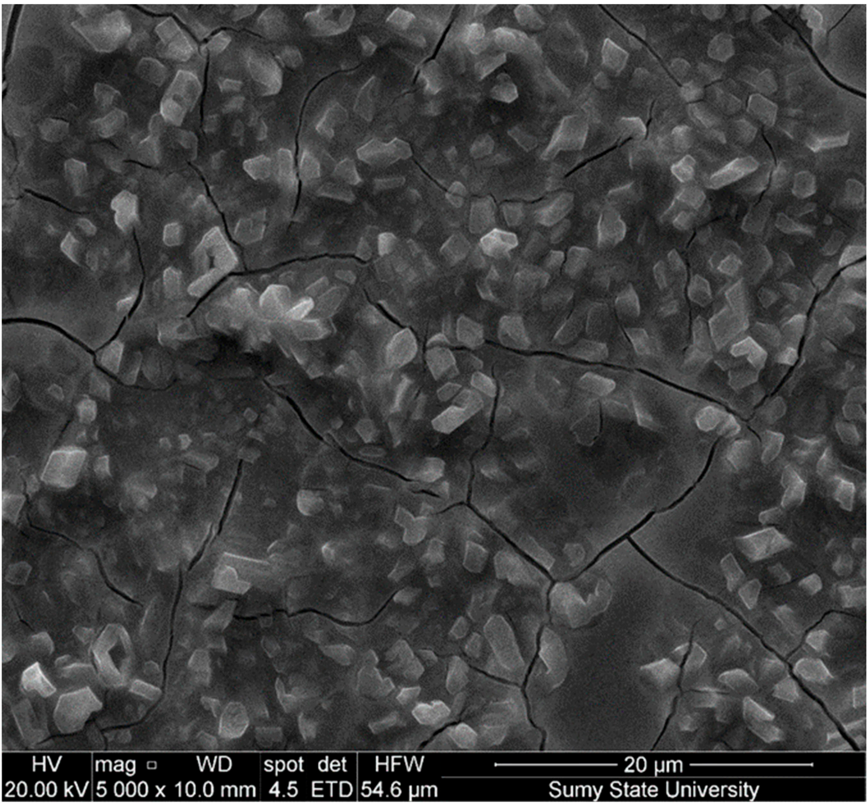

Figure 3. SEM image of the textured GaAs surface.

2.4. Electrolyte for Electrochemical Deposition of $Al_xGa_{1-x}As$

The electrochemical deposition of $Al_xGa_{1-x}As$ nanocrystallites was conducted immediately after the etching process to minimize oxidation of the etched surfaces. An aluminum chloride ($AlCl_3$) solution was used as the electrolyte. Aluminum chloride was dissolved in distilled water for a 1:1 molar concentration ratio. The solution preparation involved using a magnetic stirrer to ensure complete dissolution and homogeneity of the mixture. Dissolution was conducted at room temperature, approximately 25 °C, for 30 min. Boric acid was added as a buffering agent to stabilize the pH further and prevent any abrupt chemical shifts during the deposition process. Approximately 0.05 M of boric acid was added to the solution, providing a mildly acidic buffer to maintain a constant pH throughout the electrochemical reaction. This addition is crucial as it prevents the hydrolysis of $AlCl_3$, which could otherwise lead to the formation of hydrochloric acid, potentially disrupting the deposition process and affecting the quality of the deposited film. After preparation, the solution was immediately used in the electrochemical cell, with all manipulations performed in an inert atmosphere and the solution protected from direct light to avoid photoinduced reactions.

2.5. Electrochemical Deposition of $Al_xGa_{1-x}As$

In the experimental setup for the first batch of samples (hereafter referred to as Sample 1), a two-step voltage regime was used for the electrochemical deposition of $Al_xGa_{1-x}As$. The process began with an initial high voltage of 3 V maintained for 2 min, followed by a subsequent lower voltage of 1 V maintained for 1 min. This sequence of alternating high and low-voltage settings constituted a single deposition cycle. This cycle was repeated thrice, resulting in a total processing time of 9 min. Each cycle, combining high and low voltage phases, was designed to improve the deposition kinetics differently: the high voltage phases aimed at aggressive aluminum incorporation, while the lower voltage periods allowed material consolidation and ion diffusion.

For the second batch of samples (hereafter referred to as Sample 2), a gradually increasing voltage regime was employed to deposit $Al_xGa_{1-x}As$. This method involved continuous and smooth voltage increases over a total processing time of 9 min. The voltage started at 0.5 V and was gradually increased at a rate of 0.5 V per minute, reaching a maximum of 5 V by the end of the deposition period. The gradual voltage adjustment was intended to promote uniform film growth, facilitating the formation of substantial crystallites.

For the third batch of samples (hereafter referred to as Sample 3), a pulsed voltage regime was used to optimize the deposition process and control the morphology of the deposited layer. Deposition was performed using a sequence of voltage pulses, where a high voltage of 3 V was applied for 2 s, followed by a lower voltage of 1 V for 1 s. The total processing time for deposition was set at 9 min. Since each cycle, consisting of high and low voltage pulses, lasted 3 s, the experiment involved 180 cycles.

2.6. Characterization

Scanning electron microscopy (SEM) was applied for morphological analysis using an SEO-SEM Inspect S50-B microscope (Sumy Plant of Electronic Microscopes, Sumy, Ukraine) at 20 kV. The deposited layers were analyzed using energy-dispersive X-ray (EDX) spectroscopy for compositional analysis and material identification. X-ray diffraction (XRD) was conducted for structural analysis, utilizing a DRON-3M (Sumy State University, Sumy, Ukraine) system with unfiltered Cu Kα radiation in the 2θ angle range of 10°–80° with a step size of 0.01°. Raman measurements were performed at room temperature using a RENISHAW inVia Reflex system (Renishaw plc, Wotton-under-Edge, United Kingdom).

3. Results

3.1. SEM Analysis and Electrochemical Deposition Mechanisms

The electrochemical deposition experiments' results demonstrate that the voltage levels, voltage application duration, and the number of deposition cycles significantly influence the morphology of $Al_xGa_{1-x}As$ nanostructures on GaAs substrates. Each sample, subjected to different electrochemical conditions, exhibited distinct morphological characteristics, indicating a strong interaction between the deposition parameters and the resulting nanostructural formations (Figure 4).

3.1.1. Morphology of Sample 1 (Figure 4a,d)

Sample 1 shows an interconnected and somewhat chaotic network of thin needle-like formations. The structure, characterized by an irregular arrangement resembling a web, provides insight into the deposition conditions and mechanisms at play during the formation of this sample. The sample predominantly consists of elongated thin structures resembling needles, randomly oriented and interconnected, forming a network. The overall morphology indicates a high degree of surface roughness with numerous peaks, valleys, and a porous structure between the needle formations.

The formation mechanism of this morphology under the given electrochemical deposition conditions can be explained by several key factors. The sample was subjected to a two-step voltage regime: an initial high voltage of 3 V for 2 min and a lower 1 V for 1 min. The high voltage phase likely induced a rapid deposition rate, resulting in the swift formation of material on the substrate. At high voltages, the electrochemical reduction of ions (such as Al^{3+} and Ga^{3+}) occurs more aggressively, promoting a higher nucleation rate. The subsequent lower voltage phase allows for less aggressive deposition, facilitating some degree of consolidation while maintaining steady growth.

The initial high voltage setting causes a surge in deposition rate at the beginning of each cycle, leading to the formation of rapidly extending thin structures, such as the observed needles. These structures begin to form and extend from various nucleation sites, rapidly growing due to the high availability of ions and the electric solid field promoting ion migration and reduction.

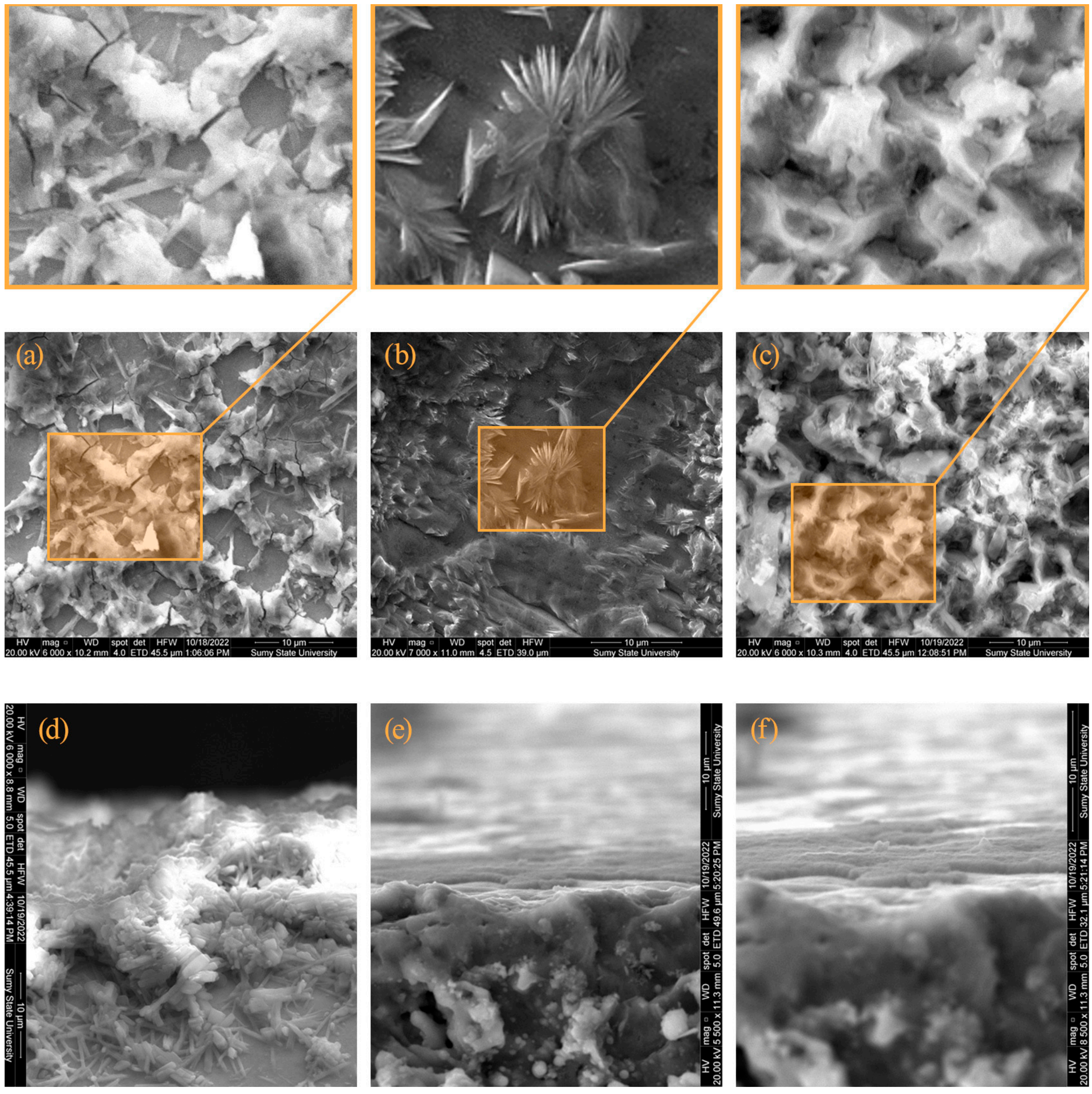

Figure 4. SEM images of surface morphology (**a**–**c**) and cross-section (**d**–**f**) of $Al_xGa_{1-x}As$ layers: (**a**,**d**)—Sample 1; (**b**,**e**)—Sample 2; (**c**,**f**)—Sample 3.

Since deposition occurs at high voltage, not all areas receive the same amount of deposited material due to variations in local electric fields, ion diffusion rates, and possibly even local fluctuations in electrolyte concentration. This results in a rough and uneven texture. The switch to lower voltage does not wholly halt growth. Still, it slows it down, allowing existing structures to become somewhat sturdier without significantly altering the overall morphology that has already formed. The interconnectedness of the needle structures suggests that as they grow, they encounter each other and merge, forming a network. This may be facilitated by solution movement or slight shifts in substrate orientation during deposition, influencing how these structures meet and interconnect.

Overall, the morphology of Sample 1 reflects the dynamic interaction between rapid nucleation and growth induced by high voltage, followed by consolidation and slower

growth at lower voltage. This sequence, repeated over three cycles, contributes to the development of the chaotic needle network observed in the SEM images, typical for materials deposited under conditions that promote rapid initial growth followed by stabilization. This morphology is advantageous for applications requiring a large surface area, although it may pose mechanical stability and uniformity challenges.

3.1.2. Morphology of Sample 2 (Figure 4b,e)

Sample 2 exhibits characteristic flower-like crystallites that are well-defined and evenly distributed across the surface. This morphology indicates controlled growth conditions and a well-managed deposition process. The structures resemble radial aggregates of crystalline petals or leaves from central nucleation points. The crystallites are uniformly distributed across the surface, suggesting a uniform ion flow and a stable electrochemical environment during deposition. The background matrix, in which these crystallites are embedded, is relatively smooth and devoid of the chaotic features seen in Sample 1, indicating controlled growth without excessive rapid deposition.

The formation of these well-defined, flower-like crystallites can primarily be attributed to the gradual voltage increase regime used during the deposition process. The process began at a lower voltage, gradually increasing over the total deposition time of 9 min. Starting at a low voltage ensures that the initial nucleation of crystallites occurs without excessively rapid ion deposition, which could lead to less ordered structures.

As the voltage gradually increases, the deposition rate also increases, but in a controlled manner. This allows the initially formed nuclei to grow outward radially, forming the petals of the flower-like structures. The gradual voltage increase ensures that each crystallite can systematically grow. Additionally, this regime controls the deposition rate and helps maintain stable ion supersaturation near the growing crystallite surfaces. This stability is crucial for the uniform growth of each crystallite.

The smooth increase in ion activity allows continuous material supply to the existing nuclei, enhancing the growth in size rather than forming new nucleation centers. The gradual voltage increase likely improves ion mobility across the substrate, ensuring that ions can reach the outer edges of the growing crystallites, supporting the formation of extended, petal-like structures.

Overall, the morphology of Sample 2, characterized by flower-like crystallites, is a direct result of methodical and controlled deposition conditions provided by the gradual voltage increase. This approach allows precise control over nucleation and growth phases, forming well-defined symmetric crystalline structures. Such structures are beneficial for applications requiring precise microstructural control and uniformity, typical for optoelectronic devices with critical stable material properties [83,84].

3.1.3. Morphology of Sample 3 (Figure 4c,f)

Sample 3 exhibits a dense porous structure with a complex rough texture. This morphology is distinct and indicates the specific influence of the deposition conditions, particularly from the use of pulsed voltage regimes.

The morphology is characterized by a very dense matrix with numerous pores. The overall structure appears compact but rough, with significant microporosity. The sample's surface is uneven and rough, with varying heights and depths along the sample. This type of texture is typical for rapid material deposition followed by periodic relaxation, allowing partial reorganization of the deposited material [85,86]. The formation of this complex porous structure can largely be explained by the electrochemical deposition conditions, particularly the pulsed voltage regime.

The deposition process utilized a pulsed voltage strategy, where high voltages alternated with lower ones. This involved setting a high voltage of 3 V for 2 s and a lower voltage of 1 V for 1 s. Such voltage pulsing promotes diverse ion deposition dynamics and substrate interactions.

During high-voltage pulses, the deposition rate significantly increases, leading to rapid material accumulation on the substrate. This rapid deposition causes an irregular and rough structure as the material has insufficient time to organize into a smoother structure.

Additionally, the pulsing nature of the voltage can cause fluctuations in local ion concentrations, resulting in uneven growth rates across the film. During the low voltage periods, the deposition rate slows, potentially allowing ions and atoms to migrate and fill some gaps, but unevenly, thereby contributing to the porous texture.

Relaxation periods (low voltage phases) allow some reorganization and settling of the deposited material, which can help create more stable junction points between grown elements. However, these periods are too short to completely smooth out the irregularities formed during the high-voltage phases, resulting in a dense but uneven texture.

Overall, the morphology of Sample 3, with its dense, porous, and rugged structure, is a direct consequence of the pulsed voltage regime used during electrochemical deposition. The alternation of high and low voltages creates a dynamic deposition environment where rapid growth phases alternate with short relaxation periods. This method promotes the development of a morphology characterized by high surface area and internal porosity, which can benefit applications requiring high reactivity or specific surface properties. However, it may pose challenges for applications requiring smooth and uniform surfaces.

3.2. EDX Analysis

Table 1 shows the elemental composition of the surface of the investigated samples. The EDX results indicate the presence of Al, Ga, and As, with varying aluminum content across the samples. It is important to note that the GaAs substrate can influence these results, especially at shallow penetration depths, characteristic of EDX analysis.

Table 1. Elemental composition of the $Al_xGa_{1-x}As$ surface, obtained using the EDX method, and the ratio of components.

Sample	Al (%)	Ga (%)	As (%)	O (%)	Ga/As	Al/Ga	(Al + Ga)/As
Sample 1	12.19	42.76	41.81	3.24	1.02	0.29	1.31
Sample 2	17.00	39.67	40.32	3.01	0.98	0.43	1.41
Sample 3	27.46	36.16	34.49	1.89	1.05	0.76	1.84

Careful sample preparation and analysis were conducted to minimize the impact of the GaAs substrate. The EDX measurements focused on areas with distinct morphological features attributable to the deposited $Al_xGa_{1-x}As$ layers. However, some Ga signals from the substrate are inevitable due to the thinness of the deposited layers. Despite this, the relative changes in Al content across the samples provide valuable insights into the deposition process and the resulting film composition.

Sample 1 had a composition of 12.19% aluminum, 42.76% gallium, 41.81% arsenic, and 3.24% oxygen. The Ga/As ratio of approximately 1.02 indicates an almost stoichiometric balance between gallium and arsenic, suggesting efficient material utilization. The Al/Ga ratio 0.29 highlights a lower aluminum incorporation level than gallium. This is corroborated by the observed needle-like chaotic morphology typically associated with rapid deposition at high voltages followed by consolidation at lower voltages. This voltage-switching regime led to swift ion deposition, forming a dense network of gallium-rich structures, as the shorter high-voltage phases were insufficient for significant aluminum incorporation.

Sample 2, formed under the gradual voltage increase regime, showed 17.00% aluminum, 39.67% gallium, 40.32% arsenic, and 3.01% oxygen. The slightly lower Ga/As ratio of 0.98 compared to Sample 1 reflects a minor deviation from stoichiometry, possibly due to a more controlled environment allowing for more uniform crystal growth. The Al/Ga ratio of 0.43 is higher than that of Sample 1, indicating more effective aluminum incorporation throughout the deposition process. This is visually confirmed by the forma-

tion of well-defined flower-like crystallites, suggesting that the gradual voltage increase promoted a stable ion flow and deposition rate conducive to structured and symmetrical crystalline forms.

Sample 3, fabricated under the pulsed voltage regime, had an elemental composition of 27.46% aluminum, 36.16% gallium, 34.49% arsenic, and 1.89% oxygen. This sample demonstrated the highest Al/Ga ratio of 0.76 among the three and a Ga/As ratio of 1.05, indicating an excess of metal cations relative to arsenic. This high aluminum content and corresponding dense, porous morphology with a rough texture can be attributed to the dynamic deposition environment created by the pulsed voltages. High-voltage pulses likely increased the aluminum deposition rate, while short relaxation periods allowed some restructuring, although insufficient to smooth the rapidly deposited layers.

While EDX analysis provides valuable insights into the elemental composition of the sample surfaces, it is essential to note its limitations. EDX only shows the percentage ratio of elements on the surface of the samples and does not allow for determining the specific compounds or their distribution within the material. We further applied XRD and Raman analyses to address these limitations and verify the presence and composition of $Al_xGa_{1-x}As$. These techniques provide more comprehensive information on the structure and crystallinity of the samples, helping to confirm the formation of the $Al_xGa_{1-x}As$ alloy and the absence of pure aluminum or other aluminum compounds.

3.3. XRD Analysis

The X-ray diffraction (XRD) spectra of the $Al_xGa_{1-x}As$ samples reveal the impact of deposition conditions on the crystalline structure and composition, which have significant implications for the material's final properties (Figure 5, Tables 2 and 3). Each sample exhibits characteristic peaks corresponding to specific crystallographic planes, systematically shifting with changes in aluminum concentration in the samples.

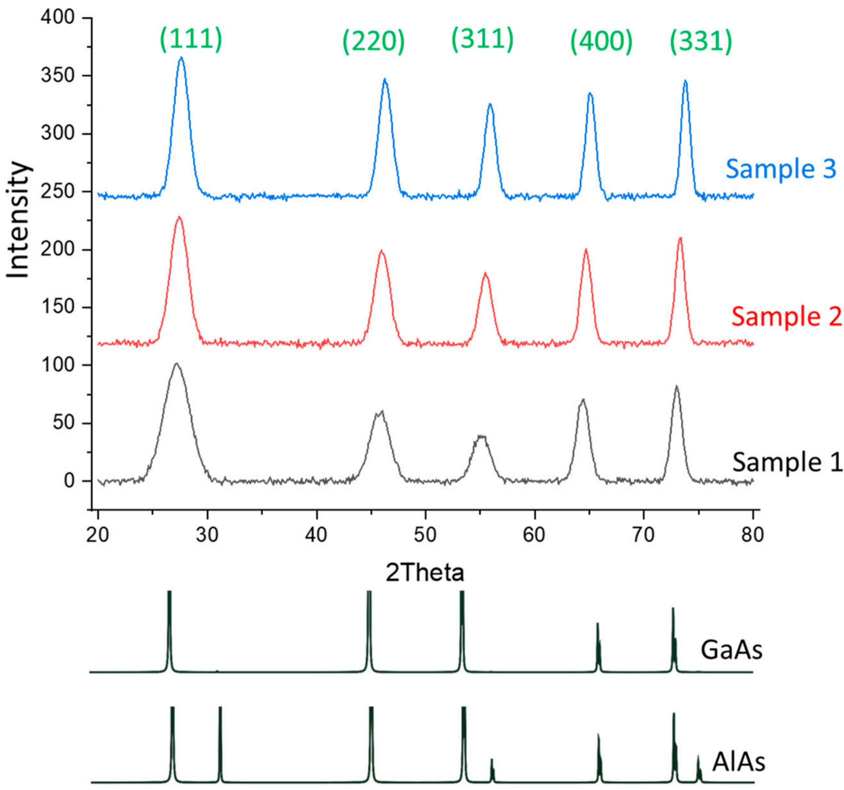

Figure 5. XRD spectra of $Al_xGa_{1-x}As$ samples with overlaid reference spectra AlAs and GaAs from the Crystallography Open Database (COD) visualized using the VESTA program.

Table 2. Positions of XRD peaks of $Al_xGa_{1-x}As$ samples.

Plane	Sample 1	Sample 2	Sample 3
(111)	27.11	27.41	27.71
(220)	46.04	45.94	46.24
(311)	55.15	55.46	55.86
(400)	64.37	64.67	65.07
(331)	72.98	73.39	73.78

Table 3. FWHM and intensity for the (111) plane peak and crystallite size.

Sample	Height, c.u.	FWHM, 2θ	d, nm
Sample 1	94.44108	2.53992	3.22
Sample 2	103.73995	1.72447	4.74
Sample 3	114.48265	1.50121	5.45

Sample 1, processed under voltage switching conditions, displayed XRD peaks at $2\theta = 27.11°$, 46.04°, 55.15°, 64.37°, and 72.98°, corresponding to the (111), (220), (311), (400), and (331) planes, respectively. These relatively broad peaks indicate reduced crystallinity and increased lattice defect presence. Broader peaks may result from aggressive etching before deposition, potentially causing non-stoichiometric gallium re-inclusion and affecting lattice order. Minimal shifts in these peak positions indicate that the lattice parameters remain relatively close to those of GaAs [87], consistent with the lower aluminum content in this sample. For instance, the (111) peak at 27.11°, the (220) peak at 46.04°, and the (400) peak at 64.37° show only minor deviations from the expected positions for GaAs, underscoring the minimal lattice distortion due to aluminum incorporation. The relatively broad FWHM observed in Sample 1 suggests significant strain or lattice defects, aligning with the discussion of aggressive etching and less controlled element re-inclusion during the voltage-switching deposition process. The intensity is the lowest among the three samples, further corroborating the notion of reduced crystallinity and increased defect density.

In contrast, Sample 2 showed sharper peaks on the same planes, reflecting a higher degree of crystallinity and reduced defect density. This sample, subjected to gradual voltage increase, likely provided a more controlled environment for aluminum integration into the gallium arsenide matrix. The inclusion of aluminum, with a smaller atomic radius than gallium, slightly contracted the lattice. This is evidenced by minor shifts toward higher angles, such as the (111) plane shifting to 27.41° and the (400) plane to 64.67°, indicating a more compact lattice structure due to the increased aluminum content. Sample 2 displays sharper peaks with a smaller FWHM than Sample 1, indicating improved crystallinity. This is likely the result of a more controlled growth environment facilitated by the gradual voltage increase during deposition. Higher peak intensity indicates better orientation and larger coherent scattering domains, corresponding to fewer defects and disruptions in the crystal lattice.

Sample 3 exhibited the most significant changes, with the sharpest and most well-defined peaks, indicating the highest crystallinity and homogeneity among the three samples. Processed using the pulsed voltage regime, this sample contained the highest aluminum level, reflected in substantial shifts of peak positions toward higher angles. For example, the (111) plane is observed at 27.71°, and the (400) plane at 65.07°. These shifts directly result from aluminum's impact on reducing the lattice constant, enhancing the material's overall electronic and optical properties. Sample 3 shows the sharpest peak and narrowest FWHM, indicating the highest level of crystallinity and uniformity among the three samples. The highest peak intensity observed here confirms the presence of highly oriented crystallites and minimal structural defects. This aligns with effective aluminum incorporation and stable crystal formation under optimized pulsed voltage conditions, resulting in a highly ordered structure.

Systematic peak angle increases from Sample 1 to Sample 3 correlate with increasing aluminum content. As aluminum replaces gallium in the crystal lattice, the overall unit cell slightly contracts due to aluminum's smaller size. This contraction shifts the diffraction angles observed in XRD analysis, providing a clear linkage between composition, crystalline structure, and the electrochemical conditions under which these materials were synthesized.

In summary, the XRD analysis demonstrates changes in crystallinity and lattice defects and vividly illustrates the impact of aluminum concentration on XRD peak shifts in various crystallographic planes. These observations are crucial for understanding the structure–property relationships essential for optimizing semiconductor device performance. The gradual improvement in FWHM and intensity from Sample 1 to Sample 3 clearly shows how electrochemical deposition parameters critically affect the crystalline quality of $Al_xGa_{1-x}As$. These enhancements correspond to the increasing aluminum content and optimized deposition conditions, improving structural order and potentially enhancing the material's electronic and optical properties. Notably, there are no peaks at 38.47°, 44.74°, 65.12°, or 78.21° (ICDD PDF 04-0787), which would indicate the presence of pure aluminum. The absence of these peaks and the observed shift in the (111) peak position confirms that aluminum is incorporated into the GaAs lattice, forming a genuine $A_{lx}Ga_{1-x}As$ alloy rather than existing as separate entities within the GaAs matrix. The correlation between sharper, more intense peaks and higher aluminum content highlights the effectiveness of controlled electrochemical conditions in achieving desired material characteristics for semiconductor applications.

3.4. Raman Analysis

Figure 6 and Table 4 present the Raman scattering spectra for the AlxGa1-xAs samples synthesized under different electrochemical conditions.

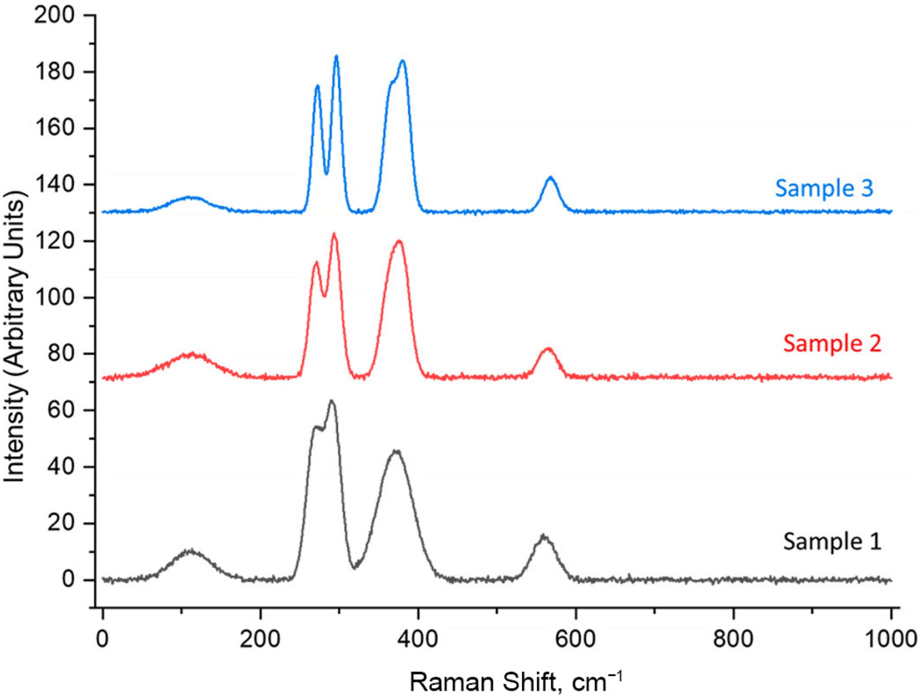

Figure 6. Raman spectra of $Al_xGa_{1-x}As$ samples.

Sample 1 showed broader peaks than the other two, indicating increased structural disorder. The Raman spectrum for this sample exhibited typical phonon modes of GaAs at 268 cm^{-1} for the transverse optical (TO) mode and 292 cm^{-1} for the longitudinal optical (LO) mode, with a noticeable shift towards broader peaks, suggesting a less homogeneous crystalline structure [88]. Additionally, the presence of peaks related to AlAs at 360 cm^{-1}

(TO) and 378 cm^{-1} (LO) indicates some degree of aluminum incorporation, although these peaks were less sharp, indicating compositional variability of the alloy [89]. A weak peak at 112 cm^{-1}, likely reflecting vibrational modes associated with defects, and a second harmonic peak at 560 cm^{-1}, indicating two LO phonon interactions, were also notable.

Table 4. The positions of Raman scattering peaks.

Sample	Peak Position (cm^{-1})		
	Sample 1	**Sample 2**	**Sample 3**
TO (GaAs)	268	270	272
LO (GaAs)	292	294	296
TO (AlAs)	360	362	364
LO (AlAs)	378	380	382
2LO (GaAs)	560	564	568
Low Frequency	112	110	110

Sample 2 showed significant improvement in peak sharpness and symmetry. This spectrum displayed sharper and more isolated phonon mode peaks at slightly shifted positions: TO and LO modes of GaAs at 270 cm^{-1} and 294 cm^{-1}, and TO and LO modes of AlAs at 362 cm^{-1} and 380 cm^{-1}. These shifts towards the frequencies of AlAs suggest a more uniform and stoichiometric incorporation of aluminum. Narrower peaks indicated reduced lattice strain and improved crystalline quality, confirmed by the reduced intensity of additional peaks at 110 cm^{-1} and 564 cm^{-1}, indicating fewer defects.

Sample 3 exhibited the highest quality Raman spectrum. Phonon mode peaks for both GaAs and AlAs were the sharpest and most symmetrical, with TO and LO modes appearing at 272 cm^{-1} and 296 cm^{-1} for GaAs, and 364 cm^{-1} and 382 cm^{-1} for AlAs, respectively. These peaks showed minimal broadening and were most distinctly shifted towards the AlAs end, confirming a higher aluminum content and an extremely homogeneous alloy composition. The additional peaks at 110 cm^{-1} and 568 cm^{-1} were minimally noticeable, emphasizing the excellent crystalline structure and reduced defect density.

The Raman spectra of our samples exhibit both GaAs-like and AlAs-like phonon modes, consistent with the expected behavior of an alloy $Al_xGa_{1-x}As$. Notably, no Raman peaks would be attributable to pure aluminum or its oxides. Pure aluminum, being a metal, does not exhibit Raman active modes under typical conditions, and the absence of peaks corresponding to aluminum oxides further confirms that aluminum is incorporated into the GaAs lattice rather than existing as separate phases. This observation, along with the characteristic dual-mode behavior of GaAs-like and AlAs-like peaks, corroborates the successful formation of $Al_xGa_{1-x}As$ alloys.

From the comprehensive analysis of the $Al_xGa_{1-x}As$ samples using Raman spectroscopy and other characterization methods, several critical observations and conclusions can be drawn, which are crucial for understanding the material properties and potential applications.

The trend from Sample 1 to Sample 3 demonstrates a clear improvement in material quality. This is evidenced by progressively sharper and more distinct Raman scattering peaks, indicating fewer crystalline defects and more excellent compositional uniformity of the alloy. These properties are essential for applications requiring high optical and electronic quality, such as optoelectronic devices and high-efficiency solar cells.

Variations in deposition conditions directly affect the crystalline structure and alloy composition. Sample 3, prepared using the shortest high-voltage pulses and the most cycles, shows the highest crystallinity and the most significant shifts in peak positions towards that characteristic of AlAs. This indicates a higher aluminum content and suggests that control over deposition parameters can be finely tuned to achieve the desired material properties.

Raman scattering spectra indicate changes in the stoichiometry of the samples. The shift towards AlAs phonon modes in Sample 3, in particular, reflects a higher aluminum content. This is beneficial for tailoring the bandgap of the material, a critical factor for semiconductor devices where bandgap engineering is necessary for specific applications.

4. Discussion

Film growth during deposition processes typically occurs through three primary mechanisms, each driven by the interaction between surface energies, adatom mobility, and film–substrate interactions [90]. Understanding these mechanisms is crucial for controlling deposited films' morphological and structural properties (Figure 7, Table 5).

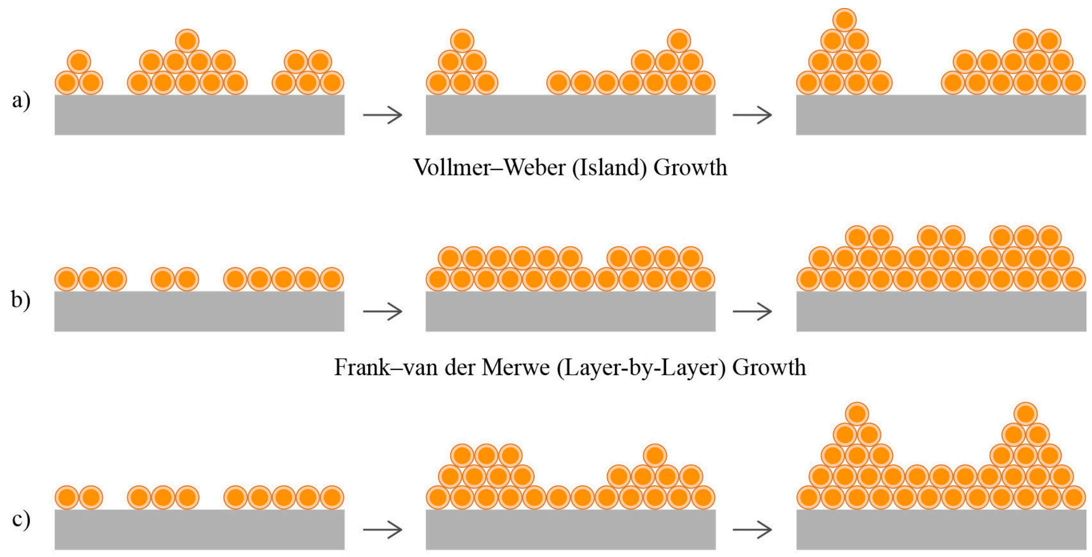

Figure 7. Schematic representation of film growth mechanisms: (**a**) WeberVollmer–Weber (Island) Growth; (**b**) Frank–van der Merwe (Layer-by-Layer) Growth; (**c**) Stranski–Krastanov (Layer-plus-Island) Growth.

Table 5. Film Growth Mechanisms.

Characteristic	Frank–van der Merwe (Layer-by-Layer) Growth	Vollmer–Weber (Island) Growth	Stranski–Krastanov (Layer-Plus-Island) Growth
Description	Complete monolayers form before the next layer starts.	Atoms/molecules form small clusters or islands.	Initial formation of monolayers, followed by island growth.
Monolayer Formation	Yes	No	Yes (initially)
Film Surface	Smooth and continuous	Rough and discontinuous	Initially smooth, then becomes rougher
Surface Roughness	Minimal	High	Intermediate
Adsorbate–Substrate Interaction	Strong	Weak	Intermediate

The Frank–van der Merwe (layer-by-layer) growth mode arises when the adhesion between the film and the substrate is stronger than the cohesion within the film itself [91]. Consequently, atoms depositing on the substrate tend to spread out and form a wetting layer, leading to film growth layer by layer. This mode is characteristic of material systems with minimal lattice mismatch and good chemical compatibility between the film and substrate [92].

In contrast, the Vollmer–Weber (island growth) mode occurs when the cohesion within the film is stronger than the adhesion to the substrate [93]. This leads to the formation of discrete material islands on the substrate, which may coalesce as the film thickness increases. This model is standard in systems with a significant lattice mismatch or poor wetting between the film and substrate [94].

The Stranski–Krastanov growth mode is a hybrid of the first two. It starts with initial layer-by-layer growth, forming a wetting layer, followed by island formation as the film thickness increases [95,96]. This mode often occurs when the film initially wets the substrate but later experiences strain due to differences in lattice parameters or thermal expansion coefficients. This leads to island formation after reaching a critical thickness [97].

In a typical scenario, given the similar lattice constants of GaAs, $Al_xGa_{1-x}As$, and AlAs [98,99], one would expect the film growth to primarily occur via the Frank–van der Merwe mode, resulting in smooth films through layer-by-layer deposition, facilitated by minimal lattice mismatch. However, introducing a textured surface significantly altered this expectation (Table 6).

Table 6. Film Growth Characteristics of $Al_xGa_{1-x}As$ Under Different Deposition Conditions.

Characteristic	Sample 1	Sample 2	Sample 3
Deposition Conditions	Two-step voltage regime: 3 V for 2 min, 1 V for 1 min.	Gradually increasing voltage: 0.5 V to 5 V over 9 min.	Pulsating voltage regime: 3 V for 2 s, 1 V for 1 s.
Morphology Description	Highly interconnected, chaotic network of delicate needle formations.	Flower-like crystallites are evenly distributed and have a smooth background matrix.	Dense porous structure with complex rough texture, underlying continuous layer.
Nucleation and Growth Dynamics	Rapid nucleation and growth at high voltage, followed by consolidation at lower voltage.	Slow, systematic nucleation at low voltage, followed by controlled growth as voltage increases.	Rapid deposition during high-voltage pulses and partial reorganization during low-voltage phases.
Surface Roughness	High	Moderate to low	High
Porosity	Present, with a highly interconnected structure.	Minimal, with well-defined crystalline structures.	Significant, with a dense and microporous structure.
Substrate Texturing Effect	Enhanced nucleation points, leading to chaotic structure.	Uniform distribution of nucleation sites, leading to symmetrical growth.	Numerous nucleation sites with high mechanical stability, contributing to rough and porous structure.
Growth Mechanism	Vollmer–Weber (Island) Growth	Stranski–Krastanov (Layer-plus-Island) Growth	Stranski–Krastanov (Layer-plus-Island) Growth with Porosity Formation

Texturing the GaAs substrates before depositing $Al_xGa_{1-x}As$ layers significantly impacted the growth mechanisms and resulting film morphology observed in the three samples. Numerous nucleation centers were introduced by electrochemically etching the GaAs surface to create a microscopically rough texture. This texturing aimed to enhance the mechanical adhesion and chemical bonding between the GaAs substrate and the $Al_xGa_{1-x}As$ layers, which is crucial for ensuring structural integrity and minimizing defects caused by lattice mismatch or thermal expansion differences.

For Sample 1, processed under a voltage-switching regime, the numerous nucleation centers created by texturing facilitated the initial rapid deposition of material at high voltages. This led to forming a highly interconnected network of thin, needle-like structures. The chaotic and dense morphology observed resulted from these conditions, promoting rapid nucleation and growth followed by some consolidation at lower voltages without smoothing the roughness. This growth mechanism aligns primarily with the Vollmer–Weber mode, characterized by island growth. The rapid deposition in high-voltage conditions conducive to the voltage-switching regime resulted in discrete nucleation centers that quickly expanded. The substrate texturing provided numerous such sites, leading to a chaotic and interconnected network of needle-like structures. While this mechanism typically suggests poor film cohesion due to island growth before coalescence, the texturing helps create more adhesion points, potentially improving the film's mechanical stability.

For Sample 2, processed using the gradual voltage increase regime, the texturing of the GaAs substrate played a crucial role in creating a controlled and uniform distribution of nucleation centers. The flower-like crystallites observed in the SEM image of this sample indicate a well-regulated growth process. Starting with a low initial voltage that gradually increased, the deposition conditions allowed slow, systematic nucleation and growth. The result was the formation of radially symmetric crystalline aggregates. This morphology, characterized by radial growth from central nucleation points, aligns with the Stranski–Krastanov growth mechanism. The initial low voltage promoted the formation of smooth, continuous layers. As the voltage gradually increased, the deposition rate also increased in a controlled manner, promoting island growth on the initial layers. The textured substrate ensured uniform growth of these islands, resulting in the observed flower-like structures. This methodical voltage increase allowed each crystallite to expand systematically, resulting in well-defined and symmetric crystalline structures.

For Sample 3, processed using the pulsed voltage regime, the resulting morphology featured a dense porous structure with a complex rough texture. The continuous layer observed in the SEM image, along with the presence of numerous pores, indicates that the growth mechanism involved forming an initial layer followed by the development of porosity due to the pulsed voltage conditions. The alternating phases of high and low voltage created a dynamic deposition environment, where rapid material deposition during high-voltage pulses was followed by partial reorganization and relaxation during low-voltage periods. This formed a continuous layer interspersed with pores, indicating a Stranski–Krastanov growth mechanism modified by subsequent etching or porosity development. High-voltage pulses promoted rapid nucleation and growth, while low-voltage phases allowed some reorganization, creating a rough and uneven surface. The GaAs substrate texturing provided numerous nucleation centers, enhancing adhesion and mechanical stability. However, the pulsed voltage regime led to a high degree of microporosity in the continuous layer, which can benefit applications requiring a large surface area and specific surface properties.

These observations highlight the versatility of wet electrochemical methods for forming $Al_xGa_{1-x}As$ films. Compared to more expensive and complex techniques, electrochemical deposition offers a range of morphologies and scales, depending on the specific deposition conditions. While these methods may lack the control of others, they allow for varying structural configurations, which is crucial for tuning the electronic and optical properties through the aluminum content (parameter x).

Adjusting x from 0 to 1 allows precise tuning of the material properties. Lower aluminum content results in properties closer to GaAs, while higher content alters the lattice constant, affecting the bandgap and other vital properties. This tunability is essential for optimizing $Al_xGa_{1-x}As$ for applications such as optoelectronic devices and high-efficiency solar cells.

Overall, the observed growth mechanisms illustrate the significant impact of substrate preparation and deposition parameters on the morphology and quality of the semiconductor film. By manipulating these parameters, manufacturers can tailor film properties to specific applications. Whether promoting smooth films or creating textured surfaces, the choice of growth mechanism directly influences the material's performance and suitability.

Nanostructured layers offer significant advantages over planar structures due to their increased surface area and unique morphological characteristics [100,101], enhancing performance in applications such as catalysis, sensor technology, energy storage, and optoelectronic devices [102–105]. Increased surface area is crucial for applications requiring high reactivity or sensitivity, such as catalysis and sensors. In energy storage and conversion, nanostructured layers facilitate faster ion transport and better interaction, improving efficiency. In optoelectronic devices, rough surfaces and complex structures manipulate light more effectively, enhancing performance.

The electrochemical method, combining substrate texturing and various voltage regimes, enhances adhesion and allows precise control over growth mechanisms, resulting

in better interface quality and fewer defects. These methods are versatile, adaptable to various materials and compositions, and scalable, making them suitable for industrial applications. Electrochemical deposition is cost-effective compared to molecular beam epitaxy or vapor phase deposition methods. It does not require high vacuum or temperatures, making it ideal for large-scale production.

Despite the thorough analysis and important observations presented in this study, some limitations should be acknowledged. Although the Raman and XRD spectra demonstrate the formation of the $Al_xGa_{1-x}As$ compound, there are still insufficient data to definitively confirm the absence of pure Al and a potential mixture of Al and GaAs. For a detailed and deep understanding of the chemical composition and structural properties, it is necessary to conduct additional research such as high-resolution transmission electron microscopy (HRTEM), X-ray photoelectron spectroscopy (XPS), and advanced photoluminescence (PL) spectroscopy. These techniques will allow us to further investigate the distribution and bonding states of aluminum in the samples, providing a more comprehensive understanding of the material's properties.

We are grateful to the reviewer for bringing this limitation to our attention, as it prompts us to conduct further research and reflection. Addressing these limitations in future studies will enhance the robustness and credibility of our findings, ensuring a thorough characterization of the $Al_xGa_{1-x}As$ compounds and their potential applications.

Future research should focus on optimizing electrochemical deposition parameters to refine further control over the morphology and properties of $Al_xGa_{1-x}As$ nanostructures. This includes exploring a more comprehensive range of voltage regimes, electrolyte compositions, and substrate texturing methods to achieve more precise tuning of aluminum content (parameter x) and its impact on electronic and optical properties.

Additionally, optical measurements are essential for a deeper understanding of the films' properties. We plan to include comprehensive optical characterization in our subsequent investigations to elucidate the optical behavior of $Al_xGa_{1-x}As$ nanostructures. This will provide critical insights into their potential applications in optoelectronics and other fields.

Moreover, investigating the scalability of these methods for industrial applications and their integration with other fabrication techniques could enhance their practicality for advanced semiconductor device manufacturing, paving the way for innovations in optoelectronics, energy conversion, and sensor technologies.

5. Conclusions

This study demonstrates the effectiveness of wet chemical synthesis for depositing $Al_xGa_{1-x}As$ nanostructures, highlighting how substrate preparation and deposition parameters significantly influence film morphology and material properties. We enhanced mechanical adhesion and chemical bonding by employing electrochemical etching to texture GaAs substrates, creating numerous nucleation centers that facilitated various growth mechanisms.

The study shows that deposition conditions critically affect sample characteristics. For example, voltage-switching regimes resulted in chaotic networks of needle-like structures, indicative of the Vollmer–Weber growth mechanism. Gradually increasing voltage regimes created well-defined flower-like crystallites, corresponding to the Stranski–Krastanov growth mechanism. Pulsed voltage regimes led to dense porous structures with continuous layers, demonstrating hybrid Stranski–Krastanov growth with additional porosity.

SEM analysis confirmed the distinct morphologies, while EDX results showed varying aluminum content reflecting changes in deposition conditions. Raman spectroscopy revealed structural disorder in samples with broader peaks and higher defect density. XRD analysis showed shifts in crystallographic peak positions corresponding to different aluminum concentrations and deposition conditions. These findings underscore the versatility of electrochemical deposition in film properties.

Our results highlight the potential of wet electrochemical methods to achieve a wide range of morphologies and compositions. Although this study focused on three specific conditions, the method allows numerous variations in processing regimes, offering a competitive advantage in tailoring $Al_xGa_{1-x}As$ films for various applications. The ability to precisely tune the aluminum content (parameter x) from 0 to 1 provides exact control over the electronic and optical properties necessary for optimizing materials for optoelectronic devices, high-efficiency solar cells, and other advanced semiconductor applications.

Overall, this work emphasizes the significant impact of deposition conditions on film characteristics and establishes wet electrochemical methods as a versatile and cost-effective approach for fabricating high-quality $Al_xGa_{1-x}As$ films with customized properties.

Author Contributions: Conceptualization, V.P., Y.S. and A.I.P.; methodology, Y.S.; software, K.K. and M.K.; validation, Y.S., K.K. and Y.Z.; formal analysis, Y.S. and Y.Z.; investigation, S.K., I.B., M.K. and Y.S.; resources, S.K. and I.B.; data curation, Y.Z., Y.S. and S.K.; writing—original draft preparation, Y.S. and V.P.; writing—review and editing, Y.S., M.K. and A.I.P.; visualization, S.K. and K.K.; supervision, A.I.P.; project administration, Y.S. and A.I.P.; funding acquisition, A.I.P. and Y.S. All authors have read and agreed to the published version of the manuscript.

Funding: This research was funded by The National Research Fund of Ukraine with the support of the University of Cambridge, Great Britain, grant number 0124U000223 "Design and Research of Oxide Heterostructures for Portable Solar Cells". In addition, the research of A.I.P. and Y.S. was partly supported by COST Action CA20129 "Multiscale Irradiation and Chemistry Driven Processes and Related Technologies" (MultIChem)., Y.S. was partly supported by COST Action CA20126 "Network for research, innovation and product development on porous semiconductors and oxides" (NETPORE). Furthermore, A.I.P was partly supported by the HORIZON 2020 RISE-RADON Project "Irradiation driven nanofabrication: computational modelling versus experiment". The Institute of Solid State Physics, University of Latvia at the Center of Excellence, has received funding from the European Union's Horizon 2020 Framework Programme H2020-WIDESPREAD-01-2016-2017-TeamingPhase2 under grant agreement No. 739508, project CAMART^2.

Data Availability Statement: The original contributions presented in the study are included in the article, further inquiries can be directed to the corresponding author/s.

Conflicts of Interest: The authors declare no conflicts of interest.

References

1. Yu, W.; Li, F.; Huang, T.; Li, W.; Wu, T. Go beyond the limit: Rationally designed mixed-dimensional perovskite/semiconductor heterostructures and their applications. *Innovation* **2022**, *4*, 100363. [CrossRef] [PubMed]
2. An, Q.; Zhang, T.; Chen, F.; Su, W. Recent progress in synthesis and physical properties of 2D ternary TMDC-based vertical heterostructures. *CrystEngComm* **2023**, *25*, 4256–4271. [CrossRef]
3. Karipbayev, Z.T.; Kumarbekov, K.; Manika, I.; Dauletbekova, A.; Kozlovskiy, A.L.; Sugak, D.; Ubizskii, S.B.; Akilbekov, A.; Suchikova, Y.; Popov, A.I. Optical, Structural, and Mechanical Properties of $Gd_3Ga_5O_{12}$ Single Crystals Irradiated with $^{84}Kr^+$ Ions. *Phys. Status Solidi B* **2022**, *259*, 2100415. [CrossRef]
4. Kovachov, S.; Bohdanov, I.; Karipbayev, Z.; Suchikova, Y.; Tsebriienko, T.; Popov, A.I. Layer-by-Layer Synthesis and Analysis of the Phase Composition of $Cd_xTe_yO_z$/CdS/por-ZnO/ZnO Heterostructure. In Proceedings of the 2022 IEEE 3rd KhPI Week on Advanced Technology (KhPIWeek), Kharkiv, Ukraine, 3–7 October 2022; IEEE: New York, NY, USA, 2022. [CrossRef]
5. Ra, H.-S.; Lee, S.-H.; Jeong, S.-J.; Cho, S.; Lee, J.-S. Advances in Heterostructures for Optoelectronic Devices: Materials, Properties, Conduction Mechanisms, Device Applications. *Small Methods* **2023**, *8*, 2300245. [CrossRef]
6. Lyu, W.; An, J.; Lin, Y.; Qiu, P.; Wang, G.; Chao, J.; Fu, B. Fabrication and Applications of Heterostructure Materials for Broadband Ultrafast Photonics. *Adv. Opt. Mater.* **2023**, *11*, 2300124. [CrossRef]
7. Sredenschek, A.J.; Sanchez, D.E.; Wang, J. Heterostructures coupling ultrathin metal carbides and chalcogenides. *Nat. Mater.* **2024**, *23*, 460–469. [CrossRef]
8. Li, X.; Aftab, S.; Abbas, A.; Hussain, S.; Aslam, M.; Kabir, F.; Abd-Rabboh, H.S.M.; Hegazy, H.H.; Xu, F.; Ansari, M.Z. Advances in Mixed 2D and 3D Perovskite Heterostructure Solar Cells: A Comprehensive Review. *Nano Energy* **2023**, *118*, 108979. [CrossRef]
9. Suchikova, Y.; Kovachov, S.; Bohdanov, I.; Karipbaev, Z.T.; Pankratov, V.; Popov, A.I. Study of the structural and morphological characteristics of the $Cd_xTe_yO_z$ nanocomposite obtained on the surface of the CdS/ZnO heterostructure by the SILAR method. *Appl. Phys. A* **2023**, *129*, 499. [CrossRef]
10. Riffat, M.; Ali, H.; Qayyum, H.A.; Bilal, M.; Hussain, T. Enhanced solar-driven water splitting by ZnO/CdTe heterostructure thin films-based photocatalysts. *Int. J. Hydrogen Energy* **2023**, *48*, 22069–22078. [CrossRef]

11. Suchikova, Y.; Kovachov, S.; Bohdanov, I.; Karipbayev, Z.T.; Zhydachevskyy, Y.; Lysak, A.; Pankratov, V.; Popov, A.I. Advanced Synthesis and Characterization of CdO/CdS/ZnO Heterostructures for Solar Energy Applications. *Materials* **2024**, *17*, 1566. [CrossRef]
12. Cheng, Z.; Wang, Y.; Zheng, R.; Mu, W. The prediction of two-dimensional PbN: Opened bandgap in heterostructure with CdO. *Front. Chem.* **2024**, *12*, 1382850. [CrossRef] [PubMed]
13. Kumar, A.S.; Wang, M.; Li, Y.; Fujita, R.; Gao, X.P.A. Interfacial Charge Transfer and Gate-Induced Hysteresis in Monochalcogenide InSe/GaSe Heterostructures. *ACS Appl. Mater. Interfaces* **2020**, *12*, 46854–46861. [CrossRef] [PubMed]
14. Kovachov, S.S.; Tikhovod, K.M.; Kalenyk, M.V.; Bohdanov, I.T.; Sychikova, Y.O. Non-Vacuum Design of $CuGa_xIn_{1-x}Se_2$ Films for Solar Energy Applications. *Met. Noveishie Tekhnol.* **2023**, *45*, 593–602. [CrossRef]
15. Suchikova, Y.; Kovachov, S.; Bohdanov, I.; Popova, E.; Moskina, A.; Popov, A. Characterization of $Cd_xTe_yO_z$/CdS/ZnO Heterostructures Synthesized by the SILAR Method. *Coatings* **2023**, *13*, 639. [CrossRef]
16. Khrypunov, G.; Vambol, S.; Deyneko, N.; Sychikova, Y. Increasing the efficiency of film solar cells based on cadmium telluride. *East.-Eur. J. Enterp. Technol.* **2016**, *6*, 12–18. [CrossRef]
17. Wang, Y.; Wang, C.; Xu, Y.; Sun, Y. Fabrication of novel Ag-doped ZnO/CdO heterostructure for high-sensitive detection of formaldehyde at low temperature. *Mater. Lett.* **2023**, *350*, 134852. [CrossRef]
18. Liu, S.; Xiao, W.; Jin, C.; Xia, S.; Wang, W.; Jiang, X.; Li, L.; Wang, S.; Chen, C. MOFs derived CdS/CdO heterojunction photoanode for high-efficient water splitting. *Appl. Surf. Sci.* **2022**, *605*, 154697. [CrossRef]
19. Bothe, K.; Bauer, G.H.; Unold, T. Spatially resolved photoluminescence measurements on $Cu(In,Ga)Se_2$ thin films. *Thin Solid Films* **2002**, *403–404*, 453–456. [CrossRef]
20. Ibragimova, S.I.; Guseinov, G.G.; Ragimov, S.S.; Asadov, Y.G. Crystal Structure and Some Physical Properties of $CuGaIn_2Se_5$. *Crystallogr. Rep.* **2019**, *64*, 883–886. [CrossRef]
21. Hoffmann, W.; Pellkofer, T. Thin films in photovoltaics: Technologies and perspectives. *Thin Solid Films* **2012**, *520*, 4094–4100. [CrossRef]
22. Romeo, A.; Artegiani, E. CdTe-Based Thin Film Solar Cells: Past, Present and Future. *Energies* **2021**, *14*, 1684. [CrossRef]
23. Genchi, G.; Sinicropi, M.S.; Lauria, G.; Carocci, A.; Catalano, A. The Effects of Cadmium Toxicity. *Int. J. Environ. Res. Public Health* **2020**, *17*, 3782. [CrossRef] [PubMed]
24. Abiodun Daramola, O.; Safari, J.B.; Adeniyi, K.O.; Siwe-Noundou, X.; Dingle, L.M.K.; Edkins, A.L.; Tseki, P.F.; Krause, R.W.M. Biocompatible liposome and chitosan-coated CdTe/CdSe/ZnSe multi-core-multi-shell fluorescent nanoprobe for biomedical applications. *J. Photochem. Photobiol. A Chem.* **2024**, *454*, 115714. [CrossRef]
25. Hu, L.; Zhong, H.; He, Z. Toxicity evaluation of cadmium-containing quantum dots: A review of optimizing physicochemical properties to diminish toxicity. *Colloids Surf. B Biointerfaces* **2021**, *200*, 111609. [CrossRef] [PubMed]
26. Fthenakis, V.; Athias, C.; Blumenthal, A.; Kulur, A.; Magliozzo, J.; Ng, D. Sustainability evaluation of CdTe PV: An update. *Renew. Sustain. Energy Rev.* **2020**, *123*, 109776. [CrossRef]
27. Li, Y.; Zhang, J.; Chen, Q.; Xia, X.; Chen, M. Emerging of Heterostructure Materials in Energy Storage: A Review. *Adv. Mater.* **2021**, *33*, 2100855. [CrossRef]
28. Sunny, F.; Subila, K.B.; Kalarikkal, N. An Overview on Lead Halide Perovskite based Composites and Heterostructures: Synthesis and Applications. *ChemNanoMat* **2023**, *10*, e202300484. [CrossRef]
29. Wu, X.; Yan, Q.; Wang, H.; Wu, D.; Zhou, H.; Li, H.; Yang, S.; Ma, T.; Zhang, H. Heterostructured Catalytic Materials as Advanced Electrocatalysts: Classification, Synthesis, Characterization, and Application. *Adv. Funct. Mater.* **2024**, 2404535. [CrossRef]
30. Acar, G.; Leguay, L.; Jones, S.; Hodgson, P.; Schliwa, A.; Hayne, M. Towards GaSb/GaAs quantum-ring single-photon LEDs: Recent progress and prospects. In Proceedings of the Light-Emitting Devices, Materials, and Applications XXVIII, San Francisco, CA, USA, 27 January–1 February 2024; Strassburg, M., Kim, J.K., Krames, M.R., Eds.; SPIE: Philadelphia, PA, USA, 2024. [CrossRef]
31. Lv, Z.; Liu, L.; Zhangyang, X.; Lu, F.; Tian, J. Comprehensive study on the optical properties of graded Al component AlxGa1-xn nanostructures for UV photocathode. *Superlattices Microstruct.* **2020**, *147*, 106695. [CrossRef]
32. Makadsi, M.N. Recent progress in epitaxial growth: GaAs, a-GaAs and a-$Al_xGa_{1-x}As$ prepared by thermal and flash evaporation. *Renew. Energy* **2003**, *28*, 155–169. [CrossRef]
33. Manfra, M.J. Molecular Beam Epitaxy of Ultra-High-Quality AlGaAs/GaAs Heterostructures: Enabling Physics in Low-Dimensional Electronic Systems. *Annu. Rev. Condens. Matter Phys.* **2014**, *5*, 347–373. [CrossRef]
34. Suchikova, Y.; Kovachov, S.; Bohdanov, I.; Abdikadirova, A.A.; Kenzhina, I.; Popov, A.I. Electrochemical Growth and Structural Study of the AlxGa1−xAs Nanowhisker Layer on the GaAs Surface. *J. Manuf. Mater. Process.* **2023**, *7*, 153. [CrossRef]
35. Koblmüller, G.; Mayer, B.; Stettner, T.; Abstreiter, G.; Finley, J.J. GaAs–AlGaAs core–shell nanowire lasers on silicon: Invited review. *Semicond. Sci. Technol.* **2017**, *32*, 053001. [CrossRef]
36. Masselink, W.T.; Chang, Y.C.; Morkoç, H.; Reynolds, D.C.; Litton, C.W.; Bajaj, K.K.; Yu, P.W. Shallow impurity levels in AlGaAs/GaAs semiconductor quantum wells. *Solid-State Electron.* **1986**, *29*, 205–214. [CrossRef]
37. Missous, M. Stoichiometric low temperature (SLT) GaAs and AlGaAs grown by molecular beam epitaxy. *Microelectron. J.* **1996**, *27*, 4–5, 393–409. [CrossRef]
38. Ueda, O. Reliability issues in III–V compound semiconductor devices: Optical devices and GaAs-based HBTs. *Microelectron. Reliab.* **1999**, *39*, 1839–1855. [CrossRef]

39. Colter, P.; Hagar, B.; Bedair, S. Tunnel Junctions for III-V Multijunction Solar Cells Review. *Crystals* **2018**, *8*, 445. [CrossRef]
40. Hansen, W. Quasi-One-Dimensional electron systems on GaAs/AlGaAs heterojunctions. In *Festkörperprobleme 28. Advances in Solid State Physics*; Rössler, U., Ed.; Springer: Berlin/Heidelberg, Germany, 1988; Volume 28. [CrossRef]
41. Kukushkin, I.; Timofeev, V.; von Klitzing, K.; Ploog, K. Magnetooptics of two-dimensional electrons under the conditions of integral and fractional quantum hall effect in Si-MOSFETs and GaAs-AlGaAs single heterojunctions. In *Festkörperprobleme 28. Advances in Solid State Physics*; Rössler, U., Ed.; Springer: Berlin/Heidelberg, Germany, 1988; Volume 28. [CrossRef]
42. Samanta, S. GaAs-based resonant tunneling diode: Device aspects from design, manufacturing, characterization and applications. *J. Semicond.* **2023**, *44*, 103101. [CrossRef]
43. Suchikova, Y. Provision of environmental safety through the use of porous semiconductors for solar energy sector. *East.-Eur. J. Enterp. Technol.* **2016**, *6*, 26–33. [CrossRef]
44. Mittal, V.; Mashanovich, G.Z.; Wilkinson, J.S. Perspective on Thin Film Waveguides for on-Chip Mid-Infrared Spectroscopy of Liquid Biochemical Analytes. *Anal. Chem.* **2020**, *92*, 10891–10901. [CrossRef]
45. Yamaguchi, M.; Araki, K.; Kojima, N.; Ohshita, Y. Overview and Loss Analysis of High-Efficiency III-V Compound Single-Junction Solar Cells. In Proceedings of the 2020 IEEE 47th Photovoltaic Specialists Conference (PVSC), Calgary, AB, Canada, 15 June–21 August 2020; IEEE: New York, NY, USA, 2020. [CrossRef]
46. Esame, O.; Gurbuz, Y.; Tekin, I.; Bozkurt, A. Performance comparison of state-of-the-art heterojunction bipolar devices (HBT) based on AlGaAs/GaAs, Si/SiGe and InGaAs/InP. *Microelectron. J.* **2004**, *35*, 901–908. [CrossRef]
47. Chou, Y.C.; Leung, D.; Grundbacher, R.; Lai, R.; Kan, Q.; Liu, P.H.; Eng, D.; Block, T.; Oki, A. Gate metal interdiffusion induced degradation in space-qualified GaAs PHEMTs. *Microelectron. Reliab.* **2006**, *46*, 24–40. [CrossRef]
48. Li, J.; Aierken, A.; Liu, Y.; Zhuang, Y.; Yang, X.; Mo, J.H.; Fan, R.K.; Chen, Q.Y.; Zhang, S.Y.; Huang, Y.M.; et al. A Brief Review of High Efficiency III-V Solar Cells for Space Application. *Front. Phys.* **2021**, *8*, 631925. [CrossRef]
49. Nanishi, Y.; Yamaguchi, T. Plasma-excited MBE—Proposal and achievements through R&D of compound semiconductor materials and devices. *Jpn. J. Appl. Phys.* **2022**, *61*, SA0810. [CrossRef]
50. Mawst, L.J.; Kim, H.; Smith, G.; Sun, W.; Tansu, N. Strained-layer quantum well materials grown by MOCVD for diode laser application. *Prog. Quantum Electron.* **2020**, *75*, 100303. [CrossRef]
51. Wang, B.; Zeng, Y.; Song, Y.; Wang, Y.; Liang, L.; Qin, L.; Zhang, J.; Jia, P.; Lei, Y.; Qiu, C.; et al. Principles of Selective Area Epitaxy and Applications in III–V Semiconductor Lasers Using MOCVD: A Review. *Crystals* **2022**, *12*, 1011. [CrossRef]
52. Hoang, A.T.; Qu, K.; Chen, X.; Ahn, J.H. Large-area synthesis of transition metal dichalcogenides via CVD and solution-based approaches and their device applications. *Nanoscale* **2021**, *13*, 615–633. [CrossRef]
53. Suchikova, Y.; Kidalov, V.; Sukach, G. Blue Shift of Photoluminescence Spectrum of Porous InP. *ECS Trans.* **2019**, *25*, 59–64. [CrossRef]
54. Althomali, R.H.; Adeosun, W.A. Wet chemically synthesized metal oxides nanoparticles, characterization and application in electrochemical energy storage: An updated review. *Synth. Met.* **2023**, *298*, 117424. [CrossRef]
55. Liu, W.; Zhang, H.; Li, C.; Wang, X.; Liu, J.; Zhang, X. Non-noble metal single-atom catalysts prepared by wet chemical method and their applications in electrochemical water splitting. *J. Energy Chem.* **2020**, *47*, 333–345. [CrossRef]
56. Suchikova, Y.O.; Kovachov, S.S.; Lazarenko, A.S.; Bardus, I.O.; Tikhovod, K.; Hurenko, O.I.; Bohdanov, I.T. Oxidation of the n-GaAs Surface: Morphological and Kinetic Analysis. *J. Nano Electron. Phys.* **2022**, *14*, 03033. [CrossRef] [PubMed]
57. Kovachov, S.; Bohdanov, I.; Bardus, I.; Drozhcha, D.; Tikhovod, K.; Khrekin, A.; Bondarenko, V.; Kosogov, I.; Suchikova, Y. About synthesis mechanism of periodic oxide nanocrystallites on surface of single-crystal InP. *Phys. Chem. Solid State* **2023**, *24*, 159–165. [CrossRef]
58. Gao, D.; Li, H.; Wei, P.; Wang, Y.; Wang, G.; Bao, X. Electrochemical synthesis of catalytic materials for energy catalysis. *Chin. J. Catal.* **2022**, *43*, 1001–1016. [CrossRef]
59. Sychikova, Y.A.; Kidalov, V.V.; Sukach, G.A. Dependence of the threshold voltage in indium-phosphide pore formation on the electrolyte composition. *J. Surf. Investig. X-ray Synchrotron Neutron Tech.* **2013**, *7*, 626–630. [CrossRef]
60. Zhang, X.; Wan, K.; Subramanian, P.; Xu, M.; Luo, J.; Fransaer, J. Electrochemical deposition of metal–organic framework films and their applications. *J. Mater. Chem. A* **2020**, *8*, 7569–7587. [CrossRef]
61. Liu, L.; Mandler, D. Using nanomaterials as building blocks for electrochemical deposition: A mini review. *Electrochem. Commun.* **2020**, *120*, 106830. [CrossRef]
62. Suchikova, Y.; Lazarenko, A.; Kovachov, S.; Usseinov, A.; Karipbaev, Z.; Popov, A.I. Formation of porous Ga_2O_3/GaAs layers for electronic devices. In Proceedings of the 2022 IEEE 16th International Conference on Advanced Trends in Radioelectronics, Telecommunications and Computer Engineering (TCSET), Lviv-Slavske, Ukraine, 22–26 February 2022; IEEE: New York, NY, USA, 2022. [CrossRef]
63. Sebastián-Pascual, P.; Jordão Pereira, I.; Escudero-Escribano, M. Tailored electrocatalysts by controlled electrochemical deposition and surface nanostructuring. *Chem. Commun.* **2020**, *56*, 13261–13272. [CrossRef] [PubMed]
64. Babu, M.A.; Varghese, A. Electrochemical deposition for metal organic Frameworks: Advanced Energy, Catalysis, sensing and separation applications. *J. Electroanal. Chem.* **2023**, *937*, 117417. [CrossRef]
65. Bernal, M.; Torres, D.; Semsari Parapari, S.; Čeh, M.; Žužek Rožman, K.; Šturm, S.; Ustarroz, J. A microscopic view on the electrochemical deposition and dissolution of Au with Scanning Electrochemical Cell Microscopy—Part I. *Electrochim. Acta* **2023**, *445*, 142023. [CrossRef]

66. Suchikova, Y.; Kovachov, S.; Bohdanov, I. Formation of oxide crystallites on the porous GaAs surface by electrochemical deposition. *Nanomater. Nanotechnol.* **2022**, *12*, 184798042211273. [CrossRef]
67. Liu, Q.F.; Meng, Z.; Hou, D.; Zhou, Y.; Cai, Y.; Zhang, M.; Tam, V.W.Y. Numerical modelling of electrochemical deposition techniques for healing concrete damaged by alkali silica reaction. *Eng. Fract. Mech.* **2022**, *276*, 108765. [CrossRef]
68. Amit, E.; Dery, L.; Dery, S.; Kim, S.; Roy, A.; Hu, Q.; Gutkin, V.; Eisenberg, H.; Stein, T.; Mandler, D.; et al. Electrochemical deposition of N-heterocyclic carbene monolayers on metal surfaces. *Nat. Commun.* **2020**, *11*, 5714. [CrossRef] [PubMed]
69. Suchikova, Y.O.; Bogdanov, I.T.; Kovachov, S.S. Oxide crystals on the surface of porous indium phosphide. *Arch. Mater. Sci. Eng.* **2019**, *2*, 49–56. [CrossRef]
70. Vambol, S.O.; Bohdanov, I.T.; Vambol, V.V.; Suchikova, Y.O.; Kondratenko, O.M.; Nestorenko, T.P.; Onyschenko, S.V. Formation of Filamentary Structures of Oxide on the Surface of Monocrystalline Gallium Arsenide. *J. Nano Electron. Phys.* **2017**, *9*, 06016. [CrossRef]
71. Tenwar, A.K.; Singh, S.; Prashant, D.V.; Samajdar, D.P. Investigation of the Optoelectronic Performance of GaAs Nanostructures Solar Cell Applications. *Mater. Today Commun.* **2022**, *33*, 104593. [CrossRef]
72. Prashant, D.V.; Agnihotri, S.K.; Bhattarai, S.; Pandey, R.; Madan, J.; Hossain, M.K.; Samajdar, D.P. Systematic Investigation of the Optoelectronic Properties of GaAs Nanowire and Nanocone Solar Cells: Effect of Geometrical Nonuniformities, Angle of Incidence, and Structural and Electronic Parameters. *ACS Appl. Electron. Mater.* **2023**, *5*, 4885–4898. [CrossRef]
73. Al-Abri, R.; Choi, H.; Parkinson, P. Measuring, controlling and exploiting heterogeneity in optoelectronic nanowires. *J. Phys. Photonics* **2021**, *3*, 022004. [CrossRef]
74. Strassner, J.; Richter, J.; Loeber, T.; Doering, C.; Fouckhardt, H. Epitaxial Growth of Optoelectronically Active Ga(As)Sb Quantum Dots on Al-Rich AlGaAs with GaAs Capsule Layers. *Adv. Mater. Sci. Eng.* **2021**, *2021*, 8862946. [CrossRef]
75. He, Y.; Tao, Y.; Liu, Z.; Huang, Q. Design and optimization of nanostructure antireflection film for thin GaAs solar cells based on the photoelectrical coupling model. *Appl. Energy* **2024**, *364*, 123184. [CrossRef]
76. Singh, S.; Mal, I.; Samajdar, D.P.; Dutta, K. Geometrical Optimization of Gallium Arsenide (GaAs) nanostructure based Solar Cells. *Mater. Today Proc.* **2022**, *58*, 686–691. [CrossRef]
77. Romeira, B.; Borme, J.; Fonseca, H.; Gaspar, J.; Nieder, J.B. Efficient light extraction in subwavelength GaAs/AlGaAs nanopillars for nanoscale light-emitting devices. *Opt. Express* **2020**, *28*, 32302. [CrossRef] [PubMed]
78. Hameed, Z.A.A.; Mutlak, F.A.H. Study the Effect of Changing the Etching Current in a Si Nanostructure to Improve the Spectral Sensitivity of the Detector. *Plasmonics* **2024**, *19*, 417–428. [CrossRef]
79. Krotkus, A.; Nevinskas, I.; Norkus, R.; Geižutis, A.; Strazdienė, V.; Pačebutas, V.; Paulauskas, T. Terahertz photocurrent spectrum analysis of AlGaAs/GaAs/GaAsBi multi-junction solar cells. *J. Phys. D Appl. Phys.* **2023**, *56*, 355109. [CrossRef]
80. Verma, A.; Pethe, A. Modelling and Analysis of Multi-Junction Photovoltaic Cells. In Proceedings of the 2020 IEEE 17th India Council International Conference (INDICON), Piscataway, NJ, USA, 10–13 December 2020; IEEE: New York, NY, USA, 2020. [CrossRef]
81. Clement, O. Crystal growth method of gallium arsenide using czochralski method. *Asian J. Multidimens. Res. (AJMR)* **2020**, *9*, 8–14. [CrossRef]
82. Rudolph, P.; Jurisch, M. Bulk growth of GaAs An overview. *J. Cryst. Growth* **1999**, *198–199*, 325–335. [CrossRef]
83. Bhojan, V.; Sebastian, A. Construction of visible-light photocatalysts through bandgap engineering. In *Advanced Functional Materials and Methods for Photodegradation of Toxic Pollutants*; Elsevier: Amsterdam, The Netherlands, 2024; pp. 63–84. [CrossRef]
84. Wang, G.; Lv, S.; Shen, Y.; Li, W.; Lin, L.; Li, Z. Advancements in heterojunction, cocatalyst, defect and morphology engineering of semiconductor oxide photocatalysts. *J. Materiomics* **2023**, *10*, 315–338. [CrossRef]
85. Kuntyi, O.; Zozulya, G.; Shepida, M. Porous Silicon Formation by Electrochemical Etching. *Adv. Mater. Sci. Eng.* **2022**, *2022*, 1482877. [CrossRef]
86. Monaico, E.I.; Monaico, E.V.; Ursaki, V.V.; Tiginyanu, I.M. Controlled Electroplating of Noble Metals on III–V Semiconductor Nanotemplates Fabricated by Anodic Etching of Bulk Substrates. *Coatings* **2022**, *12*, 1521. [CrossRef]
87. Calamiotou, M.; Raptis, Y.S.; Anastassakis, E.; Lagadas, M.; Hatzopoulos, Z. XRD and Raman studies of low-temperature-grown GaAs epilayers. *Solid State Commun.* **1993**, *87*, 563–566. [CrossRef]
88. Silva, S.W.d.; Galzerani, J.C.; Lubyshev, D.I.; Basmaji, P. Surface phonon observed in GaAs wire crystals grown on porous Si. *J. Phys. Condens. Matter* **1998**, *10*, 9687–9690. [CrossRef]
89. Efremov, M.D.; Volodin, V.A.; Sachkov, V.A.; Preobrazhenski, V.V.; Semyagin, B.R.; Ledentsov, N.N.; Ustinov, V.M.; Soshnikov, I.P.; Litvinov, D.; Rosenauer, A.; et al. Raman study of GaAs quantum wires grown with partial filling of corrugated (311)A AlAs surfaces. *Microelectron. J.* **2002**, *33*, 535–540. [CrossRef]
90. Lozovoy, K.A.; Korotaev, A.G.; Kokhanenko, A.P.; Dirko, V.V.; Voitsekhovskii, A.V. Kinetics of epitaxial formation of nanostructures by Frank–van der Merwe, Volmer–Weber and Stranski–Krastanow growth modes. *Surf. Coat. Technol.* **2020**, *384*, 125289. [CrossRef]
91. Lorenz, M.; Wei, H.; Jung, F.; Hohenberger, S.; Hochmuth, H.; Grundmann, M.; Patzig, C.; Selle, S.; Höche, T. Two-dimensional Frank–van-der-Merwe growth of functional oxide and nitride thin film superlattices by pulsed laser deposition. *J. Mater. Res.* **2017**, *32*, 3936–3946. [CrossRef]
92. Springholz, G.; Frank, N.; Bauer, G. The origin of surface roughening in lattice-mismatched Frank van der Merwe type heteroepitaxy. *Thin Solid Films* **1995**, *267*, 15–23. [CrossRef]

93. Cimalla, V.; Zekentes, K.; Vouroutzis, N. Control of morphological transitions during heteroepitaxial island growth by reflection high-energy electron diffraction. *Mater. Sci. Eng. B* **2002**, *88*, 186–190. [CrossRef]
94. Marchetto, H.; Schmidt, T.; Groh, U.; Maier, F.C.; Lévesque, P.L.; Fink, R.H.; Freund, H.-J.; Umbach, E. Direct observation of epitaxial organic film growth: Temperature-dependent growth mechanisms and metastability. *Phys. Chem. Chem. Phys.* **2015**, *17*, 29150–29160. [CrossRef] [PubMed]
95. Venäläinen, O.; Heiniö, J.; Kaski, K. Stranski-Krastanov Growth of Thin Film: Monte Carlo Simulation. *Phys. Scr.* **1991**, *T38*, 66–69. [CrossRef]
96. Wang, L.; Wang, X.; Zhao, Z.-L.; Wan, L.-J.; Wang, D. Stranski–Krastanov Growth of Two-Dimensional Covalent Organic Framework Films. *J. Am. Chem. Soc.* **2024**, *146*, 14079–14085. [CrossRef] [PubMed]
97. Yuan, H.; Chen, Y.; Lin, R.; Tan, D.; Zhang, J.; Wang, Y.; Gazit, E.; Ji, W.; Yang, R. Modified Stranski–Krastanov Growth of Amino Acid Arrays toward Piezoelectric Energy Harvesting. *ACS Appl. Mater. Interfaces* **2022**, *14*, 46304–46312. [CrossRef]
98. Boz, F.K.; Nisanci, B.; Aktas, S.; Okan, S.E. Energy levels of GaAs/$Al_xGa_{1-x}As$/AlAs spherical quantum dot with an impurity. *Appl. Surf. Sci.* **2016**, *387*, 76–81. [CrossRef]
99. Jacob, J.M.; Kim, D.S.; Bouchalkha, A.; Song, J.J.; Klem, J.F.; Hou, H.; Tu, C.W.; Morkoç, H. Spatial characteristics of GaAs, GaAs-like, and AlAs-like LO phonons in GaAs/$Al_xGa_{1-x}As$ superlattices: The strong x dependence. *Solid State Commun.* **1994**, *91*, 721–724. [CrossRef]
100. Reuter, D.; Kähler, D.; Kunze, U.; Wieck, A.D. Layer-compensated selectively doped $Al_xGa_{1-x}As$/GaAs heterostructures as a base material for nanolithography. *Semicond. Sci. Technol.* **2001**, *16*, 603–607. [CrossRef]
101. Francaviglia, L.; Fontana, Y.; Conesa-Boj, S.; Tütüncüoglu, G.; Duchêne, L.; Tanasescu, M.B.; Matteini, F.; Fontcuberta i Morral, A. Quantum dots in the GaAs/$Al_xGa_{1-x}As$ core-shell nanowires: Statistical occurrence as a function of the shell thickness. *Appl. Phys. Lett.* **2015**, *107*, 033106. [CrossRef]
102. Wilhelm, T.S.; Wang, Z.; Baboli, M.A.; Yan, J.; Preble, S.F.; Mohseni, P.K. Ordered $Al_xGa_{1-x}As$ Nanopillar Arrays via Inverse Metal-Assisted Chemical Etching. *ACS Appl. Mater. Interfaces* **2018**, *10*, 27488–27497. [CrossRef]
103. Maitra, T.; Pradhan, A.; Mukherjee, S.; Mukherjee, S.; Nayak, A.; Bhunia, S. Evaluation of spontaneous superlattice ordering in MOCVD grown $Al_xGa_{1-x}As$ epilayer on GaAs (100) using X-ray reflectivity and rocking curve analysis. *Phys. E Low-Dimens. Syst. Nanostruct.* **2019**, *106*, 357–362. [CrossRef]
104. Shen, L.-H.; Zhang, G.-L.; Yang, D.-C. Controllable GMR device in a δ-doped, magnetically and electrically modulated, GaAs/AlxGa1−xAs heterostructure. *Phys. E Low-Dimens. Syst. Nanostruct.* **2016**, *83*, 450–454. [CrossRef]
105. Maxwell Andrews, A.; Schramböck, M.; Strasser, G. InAs Quantum Dots on $Al_xGa_{1-x}As$ Surfaces and in an $Al_xGa_{1-x}As$ Matrix. In *Handbook of Self Assembled Semiconductor Nanostructures for Novel Devices in Photonics and Electronics*; Elsevier: Amsterdam, The Netherlands, 2008; pp. 62–83. [CrossRef]

Disclaimer/Publisher's Note: The statements, opinions and data contained in all publications are solely those of the individual author(s) and contributor(s) and not of MDPI and/or the editor(s). MDPI and/or the editor(s) disclaim responsibility for any injury to people or property resulting from any ideas, methods, instructions or products referred to in the content.